nature materials

ARTICLES

PUBLISHED ONLINE: 8 JUNE 2014 | DOI: 10.1038/NMAT4007

Air-stable n-type colloidal quantum dot solids

Zhijun Ning[1], Oleksandr Voznyy[1], Jun Pan[2], Sjoerd Hoogland[1], Valerio Adinolfi[1], Jixian Xu[1], Min Li[3], Ahmad R. Kirmani[2], Jon-Paul Sun[4], James Minor[1], Kyle W. Kemp[1], Haopeng Dong[1], Lisa Rollny[1], André Labelle[1], Graham Carey[1], Brandon Sutherland[1], Ian Hill[4], Aram Amassian[2], Huan Liu[3], Jiang Tang[5], Osman M. Bakr[2] and Edward H. Sargent[1]*

Colloidal quantum dots (CQDs) offer promise in flexible electronics, light sensing and energy conversion. These applications rely on rectifying junctions that require the creation of high-quality CQD solids that are controllably n-type (electron-rich) or p-type (hole-rich). Unfortunately, n-type semiconductors made using soft matter are notoriously prone to oxidation within minutes of air exposure. Here we report high-performance, air-stable n-type CQD solids. Using density functional theory we identify inorganic passivants that bind strongly to the CQD surface and repel oxidative attack. A materials processing strategy that wards off strong protic attack by polar solvents enabled the synthesis of an air-stable n-type PbS CQD solid. This material was used to build an air-processed inverted quantum junction device, which shows the highest current density from any CQD solar cell and a solar power conversion efficiency as high as 8%. We also feature the n-type CQD solid in the rapid, sensitive, and specific detection of atmospheric NO_2. This work paves the way for new families of electronic devices that leverage air-stable quantum-tuned materials.

Colloidal quantum dots have received considerable attention in the past decade owing to their promise in optoelectronic devices such as light emitting diodes[1,2], photovoltaics[3–7], photodectors[8] and field-effect transistors[9–12]. Their facile solution processing, quantum-size-effect bandgap tunability, and multi-exciton generation make them particularly attractive as the active absorbing layer in solar cells[13].

Progress in CQD solar cells—much based on the lead chalcogenide (PbS) class of materials investigated herein—has benefited from improved processes to control the doping type and density in CQD solids. Most prior solar cell work has primarily employed p-type CQD films, as these are prone to take on a p-type character when subjected even to low levels of air exposure. Both Schottky and heterojunction solar cells exploit these p-type solids[14–16]. A worldwide effort to improve device performance[17–30] has led to certified device efficiencies of a remarkable 8.6% (ref. 31)—a rapid rate of advance considering sub-1% early reports less than a decade ago.

Recently, it was recognized that having access to mutually compatible, high-performance CQDs materials of each type, p-type and n-type, would enable new classes and combinations of optoelectronic devices, such as quantum junction rectifying devices, to be formed[32–34]. In quantum junctions, each side of the junction is solar-light-absorbing, and quantum-size-effect tuning enables an inherent match between the conduction and valence bands levels on the two sides of the junction. More broadly, mutually compatible materials of each type could enable CQD complementary metal oxide semiconductor (CMOS) and advanced CQD optoelectronics, including devices such as bipolar junction transistors and multilevel logic.

Whereas large-bandgap, deep-ionization-potential, solar-transparent oxides such as ZnO and TiO_2 can be air-stable, it is unfortunately the case that smaller-bandgap processible materials with shallow ionization potentials, including chalcogenides and many organic semiconductors, are notoriously prone to oxidation. This typically results in the loss of n-type character when shallow-work-function (hence reactive) materials are exposed to air. This has been seen in the field of organic semiconductors, although this field also offers encouragement, as air-stable n-type dopants for organic materials have recently been reported[35].

Air-instability has so far characterized all n-type CQD solids employed in bipolar devices—that is, in all materials that require efficient and simultaneous extraction of both electrons and holes. Encapsulation using atomic layer deposition (ALD) has enabled operation of n-type CQD field-effect transistors in air[36]; however, until now, no unencapsulated, air-stable n-type CQD film has been reported, nor has a bipolar device been obtained. N-type CQD solids have been realized using alkali metals or radicals, metal cations, and a redox couple as the dopant[37–40]; however, once again, bipolar devices such as solar cells and diodes have yet to be reported that employ these highly reactive dopants.

We sought to realize the full potential of CQD solids for optoelectronic devices by creating an air-stable n-type material set. This would obviate the need for highly robust encapsulation. It would also enable development of new device architectures. The instability of n-type CQDs to date has, for example, required that the n-type layer constitutes the final (top) layer in the materials stack, as the p-type materials rely on air exposure to achieve their desired doping. We would seek to build devices in which the n-type and p-type quantum dot layers could be combined, within a

[1]Department of Electrical and Computer Engineering, University of Toronto, 10 King's College Road, Toronto, Ontario, M5S 3G4, Canada, [2]Division of Physical Sciences and Engineering, Solar and Photovoltaics Engineering Center, King Abdullah University of Science and Technology (KAUST), Thuwal 23955-6900, Saudi Arabia, [3]School of Optical and Electronic Information, Huazhong University of Science and Technology, 1037 Luoyu Road, Wuhan, Hubei 430074, China, [4]Dalhousie University, Department of Physics and Atmospheric Science, Rm 319 Dunn Building, Halifax, Nova Scotia, B3H 4R2, Canada, [5]Wuhan National Laboratory for Optoelectronics, Huazhong University of Sciences and Technology, 1037 Luoyu Road, Wuhan, Hubei 430074, China. *e-mail: ted.sargent@utoronto.ca

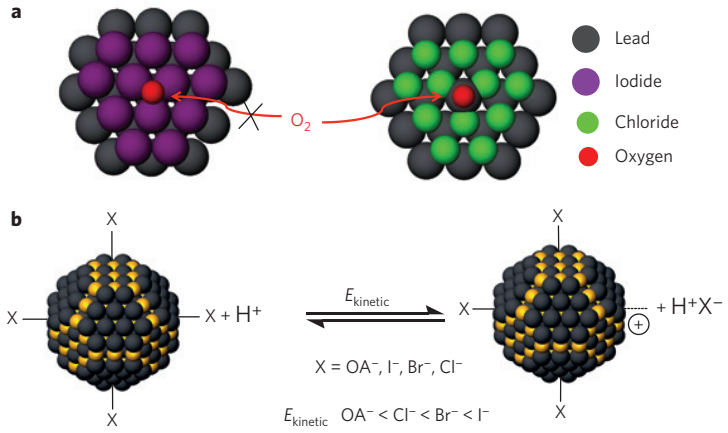

Figure 1 | Surface engineering of CQD solids for air stability. a, To realize air-stable n-type CQDs, we sought to prevent the oxidation of the electron-rich n-type CQDs. A complete and robust ligand shell would protect the surface against attack by oxygen. We selected ligands that completely passivate the dangling bonds on the CQD surface, and at the same time sterically inhibit oxidative attack. **b**, The kinetic energy ($E_{kinetic}$) of desorption of different ligands under the attack of hydrogen protons. Yellow and black spheres represent sulphur and lead atoms, respectively. To prevent desorption of halide ligands during ligand exchange, strong binding of the halides is important. Based on density functional theory simulations, the reaction kinetic energy for desorption of iodide is much higher than for chloride. OA, oleic acid.

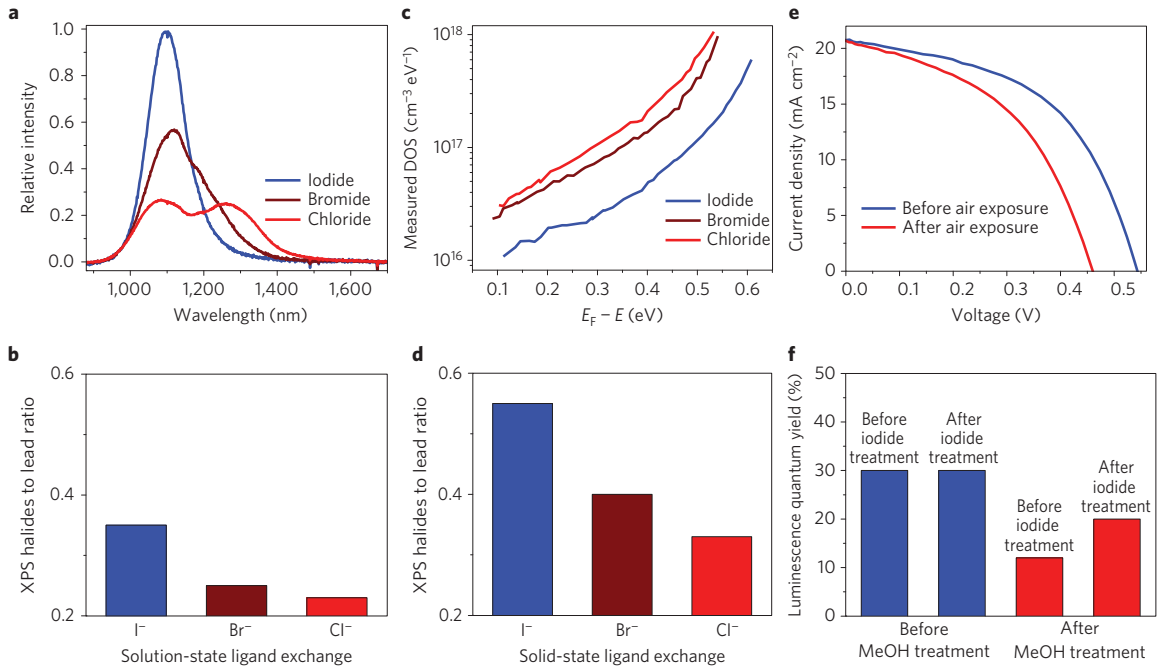

Figure 2 | Halide ligands incorporated in solution-phase and solid-state ligand exchanges. a, Photoluminescence spectra of the CQDs after solution-state halide ligands exchange. Iodide-processed CQDs show a sharp exciton emission peak, whereas bromide and chloride show side peaks in the long-wavelength region. Furthermore, the absorbance exciton peak of the chloride-treated sample is broader (Supplementary Fig. 3), also indicating the loss of ligands and the formation of defects. **b**, Atomic halide to lead ratio of the CQDs after solution-state ligand exchange. The amount of iodide ligands is much higher than chloride and bromide ligands. **c**, Defect state densities of the CQD films with different halides after solid-state ligand exchange, derived from open-circuit voltage transient decay measurements. E_F is the Fermi energy level. The defect state density in the iodide-processed film is much smaller than for films processed with chloride and bromide. **d**, Halide ligand to lead atomic ratio within the CQD films after the solid-state ligand exchange. Similarly to the solution-state ligand exchange, the amount of iodide ligands is much higher than chloride and bromide. **e**, Current–voltage curves of the device prepared by post-iodide solution-treated CQD (Method 1 in Supplementary Fig. 7). After air exposure, the open-circuit voltage and power-conversion efficiency of the device are noticeably decreased. Supplementary Table 2 shows the device performance data. **f**, Effect of halide treatment time on the photoluminescence quantum yield (PLQY) of the CQDs. The PLQY of the original CQDs before any treatment is 30%. CQDs with iodide treatment before methanol washing maintain a PLQY of 30%. However, for the methanol-treated CQDs before iodide treatment, the PLQY decreased to 12%. The post-iodine solution treatment after methanol washing increased the PLQY to 20%[45].

single compatible process environment, to create record-performing quantum junction solar cells.

We posited that adopting a complete ligand shell (Fig. 1a)—one constructed using strongly bound ligands—could protect the surfaces of CQDs from the effects of direct exposure to oxygen, and achieve air-stable CQD films without requiring encapsulation. We focused on halides, both for their n-type doping character in CQD solids[41] and for their small steric hindrance for complete coverage of

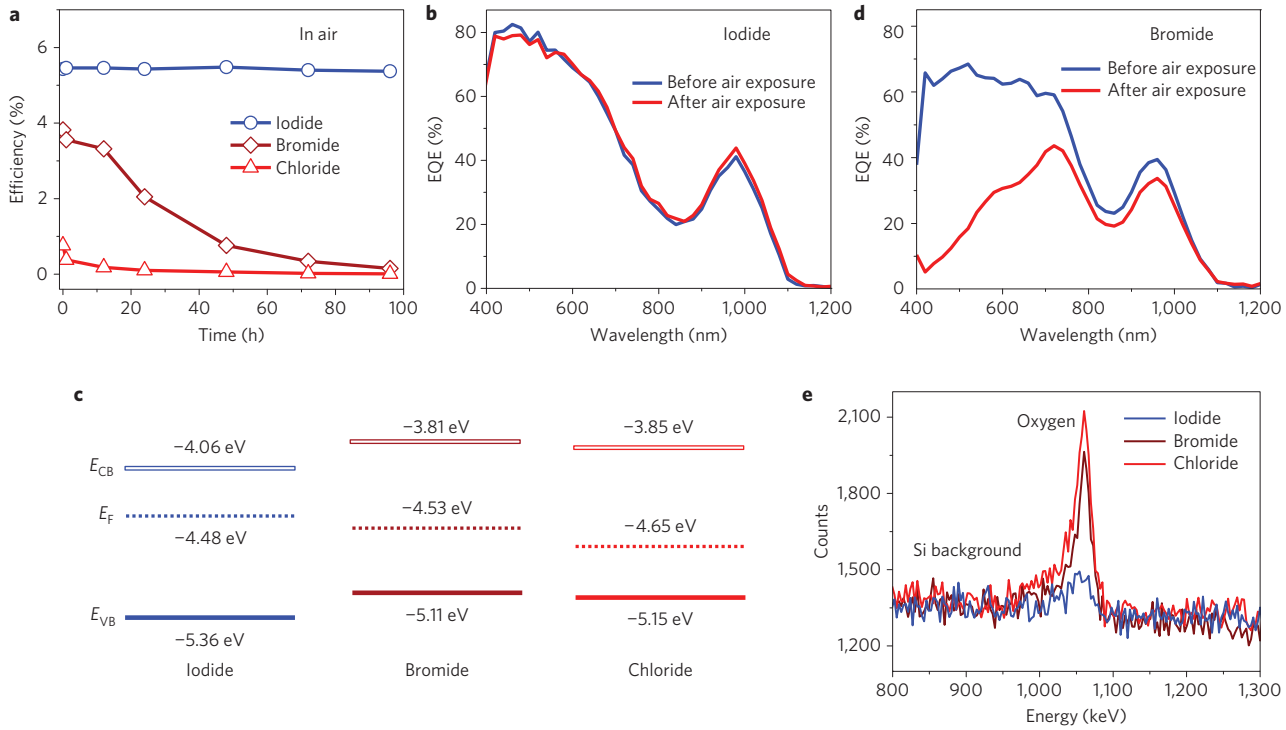

Figure 3 | Air-stable CQD solar cells. a, Efficiency of conventional quantum junction devices tested in air and followed over four days (~100 h). Iodide solid-state ligand-exchanged devices show no obvious performance change. For bromide and chloride, the device performance was significantly reduced after air exposure. Details of changes in the parameters for iodide-treated and bromide-treated films are shown in Supplementary Figs 8 and 12, respectively. **b**, External quantum efficiency (EQE) spectra of a representative iodide solid-state ligand-exchanged device. No change in the spectral shape was observed before and after air exposure. **c**, Summary of the ultraviolet photoelectron spectroscopy results: Fermi level (E_F) and valence band level (E_{VB}) of CQD films with different halide treatments. The conduction band level (E_{CB}) is calculated based on the valence band level and the CQD bandgap. All films were exposed to air before measurements. Iodide-treated films maintain their n-type character, whereas bromide-treated and chloride-treated films become p-type following air exposure. **d**, EQE spectra of the bromide solid-state-exchanged device before and after air exposure. After air exposure, the EQE value in the blue region is significantly reduced, indicating loss of the junction at the interface between the p-type and original n-type CQD layers. The results suggested that the bromide-processed n-type film was easily oxidized and converted to p-type. **e**, Rutherford backscattering spectrometry results revealing the oxide content in the film following air exposure for four days. The amounts of oxide in the bromide and chloride solid-state-exchanged film are significantly higher than for iodide, confirming the film is readily oxidized when passivated with chloride and bromide ligands.

the nanoparticle surface. We were encouraged that iodide, with its large atomic radius, could help better protect the surface of CQDs as compared to the smaller halide anions (Fig. 1a).

Achieving comprehensive coating of each nanocrystal would require a judicious choice of the ligands used to form the desired complete ligand shell as well. The fabrication of conductive CQD films relies on replacing the long alkyl ligands used in CQD synthesis with short ligands. Protic solvents are typically used to aid in desorbing the original ligands and thus present sites for binding of the final ligand. Quantum dots are particularly prone to oxidation during the course of this exchange, as evidenced by the marked reduction in photoluminescence quantum yield (PLQY) incurred during this process step[26,42]. The binding strength of the final ligands on the CQD surface is critical to preventing the loss of ligand during this process. The development of colloidal quantum dot photovoltaics has been advanced by the halide treatments in the past few years, and the performance has been continuously improving. Nevertheless, until now, the different halides have been generally considered to work similarly, with no reports that detail their differences.

We sought a predictive approach (Fig. 1b) to the design of improved passivation strategies towards air-stable n-type CQD solids by halide ligands. Using density functional theory[43], we observed that chloride ligands are indeed prone to desorption from PbS CQD surfaces under protic solvent attack. The energy to desorb iodide was 0.5 eV higher, a result consistent with hard–soft acid–base theory[44], wherein protons (the hardest acids) will bind more strongly to the hard (chloride) base than to the soft (iodide) base (Supplementary Table 1), making the chloride-terminated ligands more susceptible to protic attack. These findings are also consistent with recent observations in p-type CQD solids, where employing chloride ligands improves surface passivation[30], but is followed by loss of chloride during a (protic) wash and correspondingly increased oxidation.

We explored this picture experimentally, first comparing the photophysical properties of differently passivated PbS CQDs (Supplementary Figs 1 and 2; also see Methods). The absorption and emission spectra of CQDs do not change significantly on solution-exchange using similar quantities of the various halides investigated, and photoluminescence intensity improves for all three kinds of halides. The much-improved photoluminescence intensity suggests that the halides remedy previously unpassivated CQD surface defects[30]. In contrast, chloride- and bromide-terminated CQDs, after subsequent precipitation using ethanol[45], lost luminescence intensity and gained a red-shifted side peak (Fig. 2a). This suggests that ligands are lost and surface defects are formed on protic attack by the nonsolvent. We analysed the molar concentration of iodide and lead in solution before precipitation, then compared this with the X-ray photoelectron spectroscopy (XPS)-measured lead:iodide atomic ratio after precipitation, and determined that the added iodide is largely bonded on the CQD surface. In contrast, there is a high degree of desorption of chloride and bromide (Fig. 2b).

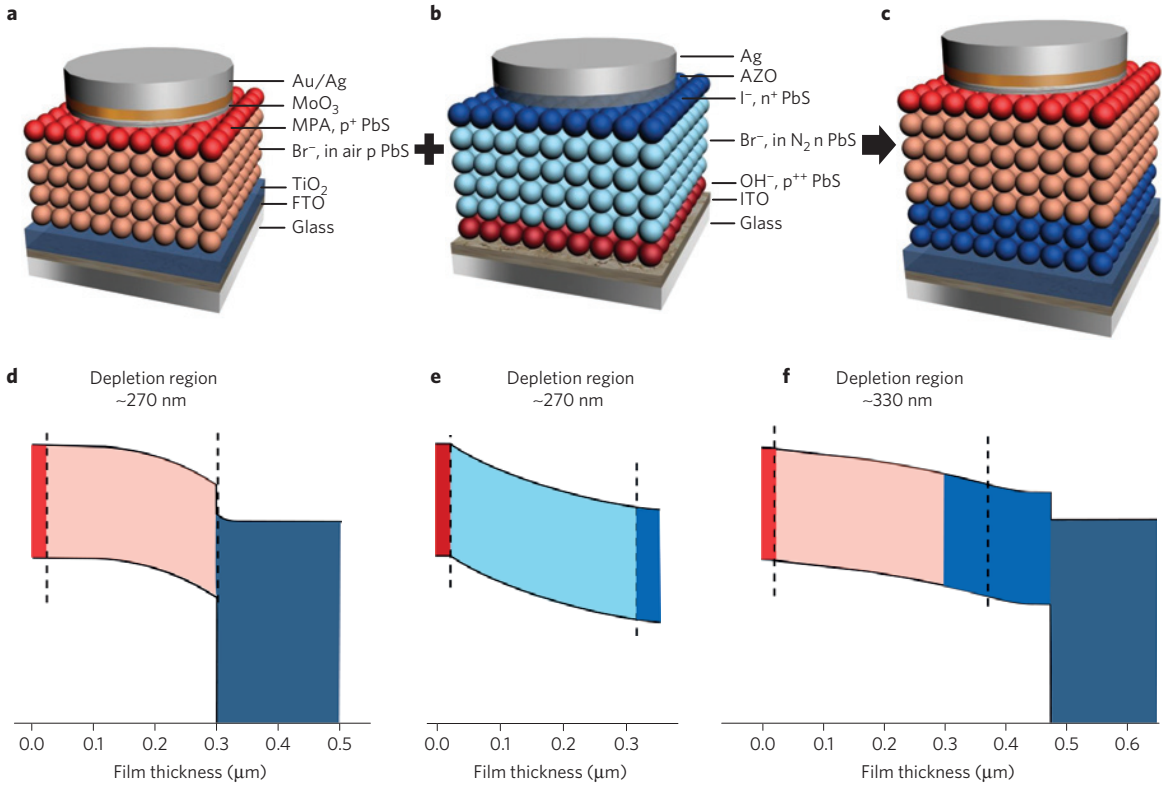

Figure 4 | Inverted quantum junction devices leverage process-compatible n- and p-type CQD solids. a–c, Schematics of heterojunction (**a**), conventional quantum junction (**b**) and inverted quantum junction (**c**) devices. Mercaptopropionic acid (MPA), bromide (Br-), iodide (I-) and hydroxide (OH-) are the ligands used for the solid-state ligand exchange in film fabrication. The inverted quantum junction device is fabricated by combining the best p-type film in the heterojunction device and the best n-type film in the quantum junction device. **d–f**, Simulated spatial band diagrams of the heterojunction (**d**), quantum junction (**e**) and inverted quantum junction (**f**) devices, operating at the maximum power point. The colours in **d–f** correspond to those of the layers used in **a–c**. The dashed lines represent the interface between adjacent layers. The depletion region of the CQD layers in the heterojunction and conventional quantum junction devices is ~270 nm. The junction and depletion region in the inverted quantum junction device is located at the interface between the n-type and p-type CQDs, and can be as large as 330 nm.

We carried out related studies of films formed from these nanoparticles. Transient photovoltage, used to quantify the density of trap states within energy gap of semiconductor solids, revealed a notably higher defect density in chloride- and bromide-treated samples compared to the iodide case (Fig. 2c; ref. 30). XPS again showed much greater retention of iodide in the films compared to the chloride and bromide cases, confirming again the more robust binding of iodide (Fig. 2d).

We then explored the stability, when operating in air, of the iodide-treated CQD solid. To do so, we constructed quantum junction solar cells (Methods), first forming a strongly p-type CQD layer via hydroxide exposure, and capping it with a much thicker n-type CQD layer[45]. For comparison, devices fabricated from conventionally treated, incompletely passivated CQDs showed near-instant loss of at least 20% of performance on air exposure (Fig. 2e; ref. 45). Films formed from CQDs that had benefited from iodide ligand exchange before any protic solvent washing (Method 2 in Supplementary Fig. 4), which had shown the significantly enhanced PLQY (Fig. 2f) and reduced trap density of states (Supplementary Figs 5 and 6), show a remarkable improvement in stability (Fig. 3a): the devices operate four days in air, under solar illumination, without loss of performance. External quantum efficiency (EQE) spectra (Fig. 3b) confirm that the devices—and their junction positions—remain unchanged on extended air exposure. Similarly, shunt and series resistances show no observable change, confirming that the quality of the rectifying junction, and thus of net doping, is preserved (Supplementary Fig. 8). The capacitance–voltage curve and field-effect transistor (FET) characteristics (Supplementary Figs 9 and 10) both confirm that the doping density of the n-type film is stable with air exposure. Ultraviolet photoelectron spectroscopy (UPS) shows that the iodide film retains its n-type character after air exposure (Fig. 3c and Supplementary Fig. 11).

In contrast, bromide- and chloride-treated devices rapidly lose performance on air exposure (Fig. 3a and Supplementary Fig. 12). EQE spectra (Fig. 3d) show a loss of performance in the blue spectral region, the EQE values decrease significantly, whereas they remain high in the infrared region, indicating that the originally n-type bromide film has turned mildly p-type, and the remaining rectification resides at the remote, now-Schottky back-side interface with the AZO top contact. FET and capacitance-voltage studies confirm this picture for both bromide (Supplementary Figs 13 and 14) and chloride (Supplementary Figs 15–17). UPS reveals that the Fermi level position of the air-exposed films has moved closer to the valence band, indicating that the bromide and chloride films have gained in p-type character as a result of air exposure (Fig. 3c and Supplementary Fig. 11). This is consistent with the decrease of open circuit voltage following air exposure in devices that employed the bromide ligand exchange (Supplementary Fig. 12). Kelvin probe measurement (Supplementary Fig. 18) confirms that bromide and chloride films show a deeper work function than iodide, consistent with the UPS results. Rutherford backscattering spectrometry (RBS) (Fig. 3e) and sputtering XPS (Supplementary Fig. 19) measurements of the films exposed to air over several days show high oxide levels throughout the film depth in the case of bromide and chloride treatments, but not in the iodide case.

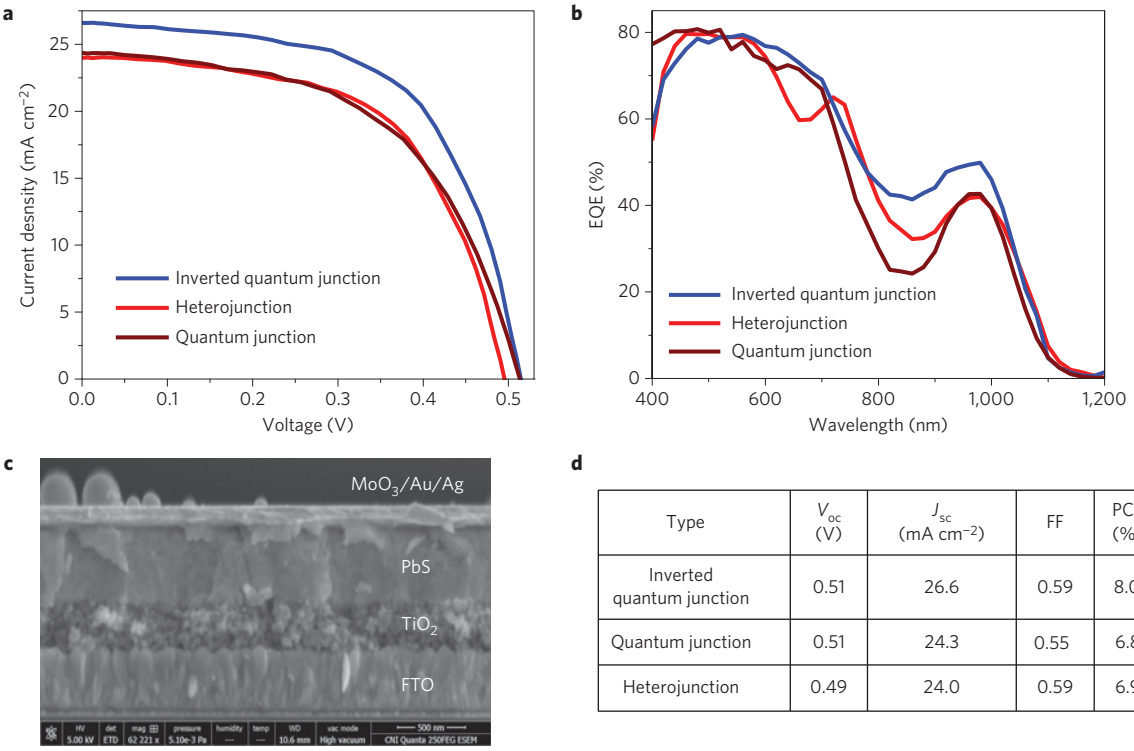

d

Type	V_{oc} (V)	J_{sc} (mA cm^{-2})	FF	PCE (%)
Inverted quantum junction	0.51	26.6	0.59	8.0
Quantum junction	0.51	24.3	0.55	6.8
Heterojunction	0.49	24.0	0.59	6.9

Figure 5 | Inverted quantum junction solar cell. a, Current–voltage curves of heterojunction, quantum junction and inverted quantum junction devices. The active layer thickness of all devices is ~450 nm. The inverted quantum junction device shows a much higher current than both the heterojunction and quantum junction devices. **b**, EQE spectra of all three devices. The inverted quantum junction device shows appreciably higher EQE values in the infrared region, which can be ascribed to its large depletion region. **c**, SEM cross-section image of the inverted quantum junction device, with an active layer thickness of ~450 nm (scale bar, 500 nm). **d**, Open-circuit voltage (V_{oc}), short-circuit density (J_{sc}), fill factor (FF) and power-conversion efficiency (PCE) for inverted quantum junction, quantum junction and heterojunction photovoltaic devices.

These findings are consistent with the stoichiometry-controlled doping framework[41], in which oxidation is predicted to convert the less-well-protected films from n-type to p-type.

We sought to showcase the benefits of air-stable n-type CQD films in a novel and beneficial device architecture. Until now, all quantum junction devices have employed a strongly p-type, air-annealed, bottom CQD layer. The hydroxyl treatment step is necessary to preserve the p-type character of the film during the ensuing inorganic n-type film deposition. Such aggressive treatment comes, however, at the cost of a very high trap density, and thus rapid recombination in the p-layer. As a result, prior quantum junction devices have had to use a thinner p-layer, thus sacrificing the current and collecting photo charge principally from the n-side.

We posited that inverting the quantum junction device structure based on a chemically- and air-stable n-type film could lead to record current densities, because it would allow a relatively thick bottom n-layer to be overcoated with a similarly thick, high-performance (low-recombination) p-layer, avoiding the undesirable hydroxyl treatment. This would be possible only if the underlying n-layer could withstand the subsequent p-layer air-atmosphere processing. Although the p-type layer can also be prepared in a glovebox using thiol ligands, exposure to air during the ligand-exchange procedure is critical to obtain the needed p-type doping density in the film (Supplementary Figs 20–22). In sum, an air-stable high-performance CQD n-layer is a prerequisite for this advantageous inverted quantum junction architecture. Other strategies have been reported that do not rely on air exposure for p-doping, such as the use of a ferrocene redox buffer[16]. However, no photoactive devices have been demonstrated using this technique: one challenge is the significant degradation of the film mobility at high doping levels.

We constructed the inverted quantum junction (Fig. 4) by depositing air-stable n-CQDs atop TiO_2 on fluoride-doped tin oxide (FTO)-coated glass; followed by lightly doped p-type film using bromide solid-state ligand exchange in air; and completed with a more heavily doped p-type layer treated using mercaptopropionic acid (MPA). Capacitance–voltage curves (Supplementary Fig. 23) confirmed that the use of the lightly doped bromide layer increased the depletion region on the p-side. The computed spatial band diagrams[46] for each device—the conventional depleted heterojunction, the previously published quantum junction, and the inverted quantum junction—are shown in Fig. 4d–f. The depletion region width inside CQD solids for both the heterojunction device and quantum junction device is about 270 nm, whereas it extends to 330 nm for the inverted quantum junction device.

Providing a thicker depletion region extends the transport length, and thus allows us to increase the CQD light-absorbing layer thickness (up to 450 nm) and thereby improve the double-pass absorption (Supplementary Fig. 24) and collected current. To ensure a fair comparison we also built depleted-heterojunction and conventional quantum junction devices having the same thickness. In both conventional devices, lower current and efficiency compared to the inverted quantum junction device were evident. The inverted quantum junction device showed a short circuit current density (J_{sc}) of 26.6 mA cm^{-2}, a record for planar CQD solar cells (Fig. 5a). The higher fill factor in the inverted quantum junction device is a further benefit of the increased depletion region at the maximum power point. The overall power-conversion efficiency of the device under AM1.5 illumination reached 8% in the best devices. A statistical analysis of 24 devices is presented in Supplementary Fig. 25. The built-in voltage of the inverted quantum junction

device reached ~0.6 V, indicating good rectification between the p-type and n-type CQDs (Supplementary Fig. 26). EQE spectra (Fig. 5b) confirm that the higher current comes from increased total absorption in the infrared spectral range. A slight decrease in EQE in the blue is consistent with the formation of the junction between n-type and p-type CQD layers. This picture is further reinforced by the observation that decreasing the thickness of the iodide n-layer increases EQE in the blue (Supplementary Fig. 27).

To illustrate the versatility of the air-stable n-type CQD films reported herein, we explored their application beyond energy capture. We reasoned that the sensing of atmospheric gases such as NO_2 requires chemically responsive electronic materials that are tolerant of (and indeed unresponsive to) the non-NO_2 components of the gas mixture under study—an ideal application for our air-stable CQD solids. We also postulated that the electron-rich n-type film could potentially see its free carrier density, and hence its conductivity, modulated by the adsorption of NO_2 on the CQD surfaces[47]. We found that the n-type CQD films, contacted using Au, normally had their current blocked by a Schottky barrier, and that the amplitude of this barrier decreased under NO_2 exposure, leading to increased current under constant bias. The resulting gas sensing proof-of-principle device exhibited rapid and stable response to NO_2 exposure (Supplementary Figs 28–31).

This work showcases a materials processing strategy that allows the construction, and the combining, of p- and n-CQD solids, independent of the order of processing. The strategy could be particularly attractive for multilayer devices in which, for example, an n-layer must be clad on each side by p-layers. Important families of devices requiring such a CQD sandwich include bipolar junction transistors; double-sided junction gate field-effect transistors (JFETs); tunnel junction devices; and all-quantum-dot tandem devices. More broadly, mutually compatible, air-stable n- and p-type layers provide a platform for active electronics and optoelectronics based on this promising, size-tuned, solution-processed family of materials.

Methods

Solution halide precursor preparation. Iodide precursor preparation: Tetrabutylammonium iodide (TBAI) was dissolved in oleylamine by heating at 200 °C for 2 h under N_2 in a Schlenk line, and then pumping for 2 h at 100 °C (10^{-3} Torr). The solution was kept at 40 °C to avoid solidification. This procedure was used to prepare a 0.6 M precursor solution obtained by dissolving TBAI (2.21 g, 6 mmol) in oleylamine (10 ml). An analogous protocol was used for the preparation of chloride and bromide precursor solutions. H^1, C^{13} nuclear magnetic resonance and mass spectroscopy of the final compounds is shown in Supplementary Information. The chemical formula is presented in Supplementary Scheme 1. The halide precursor is prepared by heating halide salts in oleylamine solution under N_2 atmosphere at 200 °C for two hours to ensure a complete reaction. *N*-butyloctadec-9-en-1-aminium iodide and tributylamine are formed after the reaction. This reaction is important for dissolving the iodide salts in oleylamine solution. The basic character of the amine precursor may reduce the content of protons in the solution and CQD surface oxidation during the ligand-exchange process. In addition, the reduced steric hindrance of the secondary amine halide compound may facilitate the ligand exchange between oleic acid and halide. The PL intensities of the CQD solutions are all increased to the same level with the addition of different halide precursors, indicating that, from the point of view of the halide–oleylamine reaction, the different halide ligands behave in a similar manner to one another (Supplementary Fig. 2).

CQD synthesis and solution halide treatment. The CQD synthesis is similar to methods reported previously[48]. Bis(trimethylsilyl) sulphide (TMS, synthesis grade) (0.18 g, 1 mol) was added to 1-octadecene (ODE) (10 ml) that had been dried and degassed by heating to 80 °C under vacuum for 24 h. A mixture of oleic acid (1.34 g, 4.8 mmol), PbO (0.45 g, 2.0 mmol) and ODE (14.2 g, 56.2 mmol) was heated to 95 °C under vacuum for 16 h and placed under Ar. The flask temperature was increased to 120 °C and the TMS/ODE mixture was injected. After injection, the flask was allowed to cool gradually to 35 °C. The nanocrystals were precipitated using distilled acetone (50 ml) and centrifuged. The supernatant was discarded and the precipitate redispersed in toluene. The nanocrystals were precipitated again using acetone (20 ml), centrifuged (5 min), dried, dispersed in toluene (50 mg ml^{-1}) and transported into a nitrogen glovebox (oxygen below 2 ppm and moisture below 10 ppm) for the solution-phase halide treatment. Iodide precursor (0.6 ml) was added to the untreated CQDs in toluene (6 ml) in a vial. The solution was stirred at room temperature for 15 min. Ethanol was added to precipitate the CQDs, and the solution was centrifuged to separate the CQDs powder from solution. The nanocrystals were finally dispersed in octane (50 mg ml^{-1}).

Film deposition for conventional quantum junction device[34]. The p-type film was prepared using the dip-coating process reported previously[34]. Indium tin oxide (ITO)-coated glass was dipped into a Ag-treated CQD (ref. 49) solution (8 mg ml^{-1}) in hexane for 20 s, and then dried in air, at room temperature for 5 min. The film was then dipped into a tetramethylammonium hydroxide solution (10 mg ml^{-1} in methanol) for 25 s, and then dried for 2 min. Finally, the film was dipped into methanol for 3 s, and dried for 200 s. This cycle was repeated three times to reach a final thickness of 30 ± 5 nm. The n-type film fabrication process is as follows: three drops of PbS CQDs (prepared based on the above CQD synthesis procedure) in octane (50 mg ml^{-1}) were deposited onto p-type film prepared above and were spin-cast at 2,500 r.p.m. for 10 s; tetrabutylammonium halides salts (30 mM) in methanol solution were deposited and left on the film for 10 s. This was followed by spinning at 2,500 r.p.m. for 10 s (repeat twice), methanol (0.5 ml) was dropped and spin-cast at 2,500 r.p.m. for 10 s (repeat twice).

A final thickness of 300 nm was achieved by depositing and treating 9–11 layers of iodide solution-treated CQDs. The n-type layer was fabricated in a nitrogen glovebox. The top electrode deposition used the same procedure as previously reported[34].

Inverted quantum junction device. TiO_2 substrates were prepared based on the procedure as reported before in reference[50]. The n-type, iodide layer preparation is similar to that detailed above for the quantum junction device. The film was prepared in a N_2 glovebox. Two to four layers of CQDs were deposited and treated to achieve a 100 ± 20 nm thickness film. The p-type, bromide-processed layer was fabricated by a similar procedure—that is 30 mM of salts in methanol, and soaked twice for 10 s. This layer was fabricated in air rather than in the glovebox, and $CdCl_2$-treated CQDs were used instead of pre-iodide solution-treated CQDs (ref. 30). This process was repeated 9–11 times to achieve a 300 ± 30 nm film (the per-layer film thickness is impacted by factors such as the temperature and humidity, and we adjusted layer number to equalize thickness). Following the bromide-treated layer, one layer of MPA solid-state-exchanged layer was deposited using the following process: two drops of $CdCl_2$ treated CQDs in octane (50 mg ml^{-1}) were spin-cast at 2,500 r.p.m. for 10 s. MPA (1% weight ratio) in methanol solution (0.25 ml) was deposited and left on the film for 3 s. This was followed by spinning at 2,500 r.p.m. for 5 s. Methanol (0.25 ml) was dropped and spin-cast at 2,500 r.p.m. for 10 s (repeat twice).

After CQD layer fabrication, the top electrode deposition used the same procedure as reported before[30].

Solar power conversion efficiency characterization. Current–voltage characteristics were measured using a Keithley 2400 sourcemeter. The air-stable quantum junction device was tested in both N_2 and air, whereas the inverted quantum junction device was tested in N_2. The solar spectrum at AM1.5 was simulated to within class A specifications (less than 25% spectral mismatch) with a Xe lamp and filters (Solar Light Company) with a measured intensity at 100.6 mW cm^{-2}. The source intensity was measured using a Melles–Griot broadband powermeter through a circular 0.102 cm^2 aperture at the position of the device and confirmed with a calibrated reference solar cell (Newport). The accuracy of the power measurement was estimated to be ±5%.

X-ray photoelectron spectroscopy and Rutherford backscattering spectrometry (RBS) analysis. XPS analysis was carried out using the Thermo Scientific K-Alpha XPS system with an Ar ion gun. Films for XPS measurements were capped with a 30 nm Ag layer to protect them from surface oxidation during sample transfer. Before XPS analysis, the Ag capping and ~100 nm of the CQD film were sputtered off to characterize the composition inside the film. RBS was performed at the Tandetron facility at the University of Western Ontario. Halide-treated CQD films of 300 nm thickness were deposited on HF-treated Si substrates. A beam energy of 3,030 keV, which is resonant with oxygen, and a dose of 10 μC were used in the analysis presented herein.

Received 22 October 2013; accepted 2 May 2014; published online 8 June 2014

References

1. Shirasaki, Y., Supran, G. J., Bawendi, M. G. & Bulovic, V. Emergence of colloidal quantum-dot light-emitting technologies. *Nature Photon.* **7,** 13–23 (2013).

2. Sun, L. *et al.* Bright infrared quantum-dot light-emitting diodes through inter-dot spacing control. *Nature Nanotech.* **7,** 369–373 (2012).
3. Tang, J. *et al.* Colloidal-quantum-dot photovoltaics using atomic-ligand passivation. *Nature Mater.* **10,** 765–771 (2011).
4. Wang, X. *et al.* Tandem colloidal quantum dot solar cells employing a graded recombination layer. *Nature Photon.* **5,** 480–484 (2011).
5. Luther, J. M. *et al.* Schottky solar cells based on colloidal nanocrystal films. *Nano Lett.* **8,** 3488–3492 (2008).
6. Brown, P. R. *et al.* Improved current extraction from ZnO/PbS quantum dot heterojunction photovoltaics using a MoO_3 interfacial layer. *Nano Lett.* **11,** 2955–2961 (2011).
7. Ma, W. *et al.* Photovoltaic performance of ultrasmall PbSe quantum dots. *ACS Nano* **5,** 8140–8147 (2011).
8. Konstantatos, G. *et al.* Ultrasensitive solution-cast quantum dot photodetectors. *Nature* **442,** 180–183 (2006).
9. David, K. K., Lai, Y., Diroll, B. T., Murray, C. B. & Kagan, C. R. Flexible and low-voltage integrated circuits constructed from high-performance nanocrystal transistors. *Nature Commun.* **3,** 1216 (2012).
10. Lee, J. S., Kovalenko, M. V., Huang, J., Chung, D. S. & Talapin, D. V. Band-like transport, high electron mobility and high photoconductivity in all-inorganic nanocrystal arrays. *Nature Nanotech.* **6,** 348–352 (2011).
11. Choi, J. H. *et al.* Bandlike transport in strongly coupled and doped quantum dot solids: A route to high-performance thin-film electronics. *Nano Lett.* **12,** 2631–2638 (2012).
12. Choi, J. H. *et al. In-situ* repair of high-performance, flexible nanocrystal electronics for large-area fabrication and operation in air. *ACS Nano* **7,** 8275–8283 (2013).
13. Sargent, E. H. Colloidal quantum dot solar cells. *Nature Photon.* **6,** 133–135 (2012).
14. Johnston, K. W. *et al.* Schottky-quantum dot photovoltaics for efficient infrared power conversion. *Appl. Phys. Lett.* **92,** 151115 (2008).
15. Pattantyus-Abraham, A. G. *et al.* Depleted-heterojunction colloidal quantum dot solar cells. *ACS Nano* **4,** 3374–3380 (2010).
16. Engel, J. H., Surendranath, Y. & Alivisatos, A. P. Controlled chemical doping of semiconductor nanocrystals using redox buffers. *J. Am. Chem. Soc.* **134,** 13200–13203 (2012).
17. Chang, L-Y., Lunt, R. R., Brown, P. R., Bulović, V. & Bawendi, M. G. Low-temperature solution-processed solar cells based on PbS colloidal quantum dot/CdS heterojunctions. *Nano Lett.* **13,** 994–999 (2013).
18. Osedach, T. P. *et al.* Bias-stress effect in 1, 2-ethanedithiol-treated PbS quantum dot field-effect transistors. *ACS Nano* **6,** 3121–3127 (2012).
19. Zhao, N. *et al.* Colloidal PbS quantum dot solar cells with high fill factor. *ACS Nano* **4,** 3743–3752 (2010).
20. Jean, J. *et al.* ZnO Nanowire arrays for enhanced photocurrent in PbS quantum dot solar cells. *Adv. Mater.* **25,** 2790–2796 (2013).
21. Strasfeld, D. B., Dorn, A., Wanger, D. D. & Bawendi, M. G. Imaging Schottky barriers and ohmic contacts in PbS quantum dot devices. *Nano Lett.* **12,** 569–575 (2012).
22. Luther, J. M. & Pietryga, J. M. Stoichiometry control in quantum dots: A viable analog to impurity doping of bulk materials. *ACS Nano* **7,** 1845–1849 (2013).
23. Lan, X. *et al.* Self-assembled, nanowire network electrodes for depleted bulk heterojunction solar cells. *Adv. Mater.* **25,** 1769–1773 (2013).
24. Luther, J. M. *et al.* Stability assessment on a 3% bilayer PbS/ZnO quantum dot heterojunction solar cell. *Adv. Mater.* **22,** 3704–3707 (2013).
25. Nozik, A. J. *et al.* Semiconductor quantum dots and quantum dot arrays and applications of multiple exciton generation to third-generation photovoltaic solar cells. *Chem. Rev.* **110,** 6873–6890 (2010).
26. Scheele, M. *et al.* Nonmonotonic size dependence in the hole mobility of methoxide-stabilized PbSe quantum dot solids. *ACS Nano* **7,** 6774–6781 (2013).
27. Ma, W., Luther, J. M., Zheng, H., Wu, Y. & Alivisatos, A. P. Photovoltaic devices employing ternary PbS_xSe_{1-x} nanocrystals. *Nano Lett.* **9,** 1699–1703 (2009).
28. Engel, J. & Alivisatos, A. P. Postsynthetic doping control of nanocrystal thin films: Balancing space charge to improve photovoltaic efficiency. *Chem. Mater.* **26,** 153–162 (2014).
29. Ning, Z. *et al.* Wave-function engineering of CdSe/CdS Core/Shell quantum dots for enhanced electron transfer to a TiO_2 Substrate. *J. Phys. Chem. C* **114,** 15184–15189 (2010).
30. Ip, A. H. *et al.* Hybrid passivated colloidal quantum dot solids. *Nature Nanotech.* **7,** 577–582 (2012).
31. Research Cell Efficiency Records by National Renewable Energy Laboratory, version at November 2013. http://www.nrel.gov/ncpv/images/efficiency_chart.jpg
32. Zhitomirsky, D. *et al.* N-type colloidal-quantum-dot solids for photovoltaics. *Adv. Mater.* **24,** 6181–6185 (2012).
33. Tang, J. *et al.* Quantum junction solar cells. *Nano Lett.* **12,** 4889–4894 (2012).
34. Ning, Z. *et al.* Graded doping for enhanced colloidal quantum dot photovoltaics. *Adv. Mater.* **25,** 1719–1723 (2013).
35. Wei, P., Oh, J. H., Dong, G. F. & Bao, Z. Use of a 1H-benzoimidazole derivative as an n-type dopant and to enable air-stable solution-processed n-channel organic thin-film transistors. *J. Am. Chem. Soc.* **132,** 8852–8853 (2010).
36. Liu, Y. PbSe Quantum dot field-effect transistors with air-stable electron mobilities above 7 $cm^2\ V^{-1}\ s^{-1}$. *Nano Lett.* **13,** 1578–1587 (2013).
37. Shim, M. & Guyot-Sionnest, P. n-type colloidal semiconductor nanocrystals. *Nature* **407,** 981–983 (2000).
38. Talapin, D. V. & Murray, C. B. PbSe nanocrystal solids for n- and p-channel thin film field-effect transistors. *Science* **310,** 86–89 (2005).
39. Mocatta, D. *et al.* Heavily doped semiconductor nanocrystal quantum dots. *Science* **332,** 77–81 (2011).
40. Koh, W-k. *et al.* Heavily doped n-type PbSe and PbS nanocrystals using ground-state charge transfer from cobaltocene. *Sci. Rep.* **3,** 2004 (2013).
41. Voznyy, O. *et al.* Charge-orbital balance picture of doping in colloidal quantum dot solids. *ACS Nano* **6,** 8448–8455 (2012).
42. Hassinen, A. *et al.* Short-chain alcohols strip X-type ligands and quench the luminescence of PbSe and CdSe quantum dots, acetonitrile does not. *J. Am. Chem. Soc.* **134,** 20705–20712 (2012).
43. Vande Vondele, J. *et al.* Quickstep: Fast and accurate density functional calculations using a mixed Gaussian and plane waves approach. *Comput. Phys. Commun.* **167,** 103–128 (2005).
44. Pearson, R. G. Hard and soft acids and bases. *J. Am. Chem. Soc.* **85,** 3533–3539 (1963).
45. Ning, Z. *et al.* All-inorganic colloidal quantum dot photovoltaics employing solution-phase halide passivation. *Adv. Mater.* **24,** 6295–6299 (2012).
46. Burgelman, M., Nollet, P. & Degrave, S. Modelling polycrystalline semiconductor solar cells. *Thin Solid Films* **361–362,** 527–532 (2000).
47. Liu, H. *et al.* Tin oxide films for nitrogen dioxide gas detection at low temperatures. *Sens. Actuat. B* **177,** 460–466 (2013).
48. Barkhouse, D. A. R. *et al.* Depleted bulk heterojunction colloidal quantum dot photovoltaics. *Adv. Mater.* **23,** 3134–3138 (2011).
49. Liu, H. *et al.* Systematic optimization of quantum junction colloidal quantum dot solar cells. *Appl. Phys. Lett.* **101,** 151112 (2012).
50. Liu, H. *et al.* Electron acceptor materials engineering in colloidal quantum dot solar cells. *Adv. Mater.* **23,** 3832–3837 (2011).

Acknowledgements

This publication is based in part on work supported by Award KUS-11-009-21, made by King Abdullah University of Science and Technology (KAUST), by the Ontario Research Fund—Research Excellence Program, and by the Natural Sciences and Engineering Research Council (NSERC) of Canada. We thank Angstrom Engineering, and Innovative Technology, for useful discussions regarding material deposition methods and control of the glovebox environment, respectively. Computations were performed using the BlueGene/Q supercomputer at the SciNet HPC Consortium provided through the Southern Ontario Smart Computing Innovation Platform (SOSCIP). The SOSCIP consortium is funded by the Ontario Government and the Federal Economic Development Agency for Southern Ontario. H.D. would like to acknowledge financial support from the China Scholarship Council (CSC). The authors thank Larissa Levina for the assistance with CQDs synthesis, S. M. Thon, A. H. Ip and M. Adachi for helpful discussions, S. Masala and J. McDowell for measurement assistance, and E. Palmiano, R. Wolowiec and D. Kopilovic for their help during the course of study. We thank L. Goncharova for assistance with RBS measurements.

Author contributions

Z.N., O.V., O.M.B. and E.H.S. designed and directed this study, analysed the results, and co-wrote the manuscript. Z.N. contributed to all experimental work. O.V. carried out the density functional theory simulations and XPS measurements. J.P, J.X. and H.D. assisted in device fabrication. S.H. and J.M. performed transient photovoltage experiments. V.A carried out optoelectronic simulations. M.L., H.L. and J.T. performed NO_2 gas sensing measurements. K.W.K., L.R., A.L., G.C. and B.S. carried out fabrication and device characterization of specific devices. A.R.K. and A.A. performed UPS measurement. J-P.S. and I.H. carried out the Kelvin probe study.

Additional information

Supplementary information is available in the online version of the paper. Reprints and permissions information is available online at www.nature.com/reprints. Correspondence and requests for materials should be addressed to E.H.S.

Competing financial interests

The authors declare no competing financial interests.